atmosphere

MDPI

Article

A Method for Retrieving Stratospheric Aerosol Extinction and Particle Size from Ground-Based Rayleigh-Mie-Raman Lidar Observations

Jacob Zalach [1,*], Christian von Savigny [1], Arvid Langenbach [2], Gerd Baumgarten [2], Franz-Josef Lübken [2] and Adam Bourassa [3]

1 Institute of Physics, University of Greifswald, Felix-Hausdorff-Str. 6, 17489 Greifswald, Germany; vonsavignc@uni-greifswald.de
2 Leibniz-Institute of Atmospheric Physics, Schlossstr. 6, 18225 Kühlungsborn, Germany; langenbach@iap-kborn.de (A.L.); baumgarten@iap-kborn.de (G.B.); franz-josef.luebken@uni-rostock.de (F.-J.L.)
3 Department of Physics & Engineering Physics, University of Saskatchewan, 116 Science Place, Saskatoon, SK S7N 5E2, Canada; adam.bourassa@usask.ca
* Correspondence: jacob.zalach@ruhr-uni-bochum.de

Received: 27 May 2020; Accepted: 17 July 2020; Published: 22 July 2020

Abstract: We report on the retrieval of stratospheric aerosol particle size and extinction coefficient profiles from multi-color backscatter measurements with the Rayleigh–Mie–Raman lidar operated at the Arctic Lidar Observatory for Middle Atmosphere Research (ALOMAR) in northern Norway. The retrievals are based on a two-step approach. In a first step, the median radius of an assumed monomodal log-normal particle size distribution with fixed width is retrieved based on a color index formed from the measured backscatter ratios at the wavelengths of 1064 nm and 532 nm. An intrinsic ambiguity of the retrieved aerosol size information is discussed. In a second step, this particle size information is used to convert the measured lidar backscatter ratio to aerosol extinction coefficients. The retrieval is currently based on monthly-averaged lidar measurements and the results for March 2013 are discussed. A sensitivity study is presented that allows for establishing an error budget for the aerosol retrievals. Assuming a monomodal log-normal aerosol particle size distribution with a geometric width of $S = 1.5$, median radii on the order of below 100 nm are retrieved. The median radii are found to generally decrease with increasing altitude. The retrieved aerosol extinction profiles are compared to observations with the OSIRIS (Optical Spectrograph and InfraRed Imager System) and the OMPS-LP (Ozone Mapping Profiling Suite Limb Profiler) satellite instruments in the 60° N to 80° N latitude band. The extinction profiles that were retrieved from the lidar measurements show good agreement with the observations of the two satellite instruments when taking the different wavelengths of the instruments into account.

Keywords: stratospheric aerosols; high latitude stratosphere; multi-wavelength lidar measurements

1. Introduction

Stratospheric aerosols are of crucial importance for various physical and chemical processes in the Earth's atmosphere [1,2]. According to the current understanding, the main component of stratospheric aerosols consists of sub-micron particles that are made of H_2SO_4 and H_2O. The stratospheric sulfate aerosol layer is thought to be maintained under volcanically quiescent conditions by a continuous influx of OCS from the troposphere [3]. Volcanic eruptions may lead to stratospheric injections of sulfur compounds, which can be photochemically converted to H_2SO_4 and contribute to the formation and growth of sulfate aerosol particles [4]. Meteoric cores are frequently found as a component of

stratospheric sulfate aerosols at high latitudes (e.g., Curtius et al. [5]). Meteoric smoke particles also play an essential role for the formation of noctilucent clouds (or polar mesospheric clouds), which are water ice clouds near the polar summer mesopause [5].

Stratospheric sulfate aerosols scatter incoming solar radiation and also absorb and re-emit terrestrial thermal radiation [6]. The net effect of an enhanced stratospheric sulfate aerosol loading is generally a surface cooling [7]. Stratospheric sulfate aerosols also provide surfaces for heterogeneous chemical reactions. For an anthropogenically enhanced stratospheric halogen loading, an increase of the aerosol surface area leads to a net catalytic destruction of stratospheric ozone [8]. This effect will be reversed, once the stratospheric halogen load has returned to background levels (e.g., [9]). In polar regions, stratospheric aerosols provide condensation nuclei for polar stratospheric clouds (PSC), which facilitate heterogeneous chemical reactions that lead to chlorine activation, in turn leading to catalytic ozone loss [10].

Up to now, lidar observations of stratospheric aerosols were essentially limited to mid-latitudes. The atmosphere in the Arctic region is much less explored and exhibits characteristic variations of its aerosol load as well as its thermal, dynamic, and chemical properties. In the current study, observations of stratospheric aerosols obtained by measurements with the Rayleigh–Mie–Raman–lidar (RMR-lidar) at the ALOMAR (Arctic Lidar Observatory for Atmospheric Research) station [11] located at 16.0° E, 69.3° N are analysed. We extend the methods used for the study of polar stratospheric clouds (PSC) to the much smaller signals of the stratospheric aerosol [12,13].

The number of experimental studies on the size of stratospheric sulfate aerosols at high latitudes is quite limited and the published stratospheric aerosol size parameters in general cover quite a large range of values, even under background aerosol conditions (see, e.g., [14]). A major advantage of this new method is that the lidar ratio does not have to be assumed, but it is calculated from the measurements themselves. For most other lidar studies on stratospheric aerosols, the value of the lidar ratio is determined based on a priori assumptions on the aerosol particle size distribution. In addition, the lidar ratio is usually assumed to be independent of altitude, which is generally not true.

To our best knowledge, the approach employed here—i.e., the retrieval of aerosol particle size information in a first step, followed by calculating extinction coefficients—has not yet been applied to lidar measurements of stratospheric sulfate aerosols.

The paper is structured, as follows. Section 2 provides a brief description of the lidar system whose measurements are used in the present study. In Section 3, we describe the steps of the retrieval approach employed to, first, obtain information on the aerosol particle size and, second, to calculate the lidar ratio and retrieve the aerosol extinction coefficient and number density profiles. The retrieval errors are discussed in Section 4 and the inferred aerosol extinction coefficient profiles are compared with satellite-borne limb-scatter measurements in Section 5. Conclusions are presented in the final Section 6.

2. The ALOMAR Rayleigh-Mie-Raman (RMR) Lidar

The RMR-lidar is based on two Nd-YAG power lasers, each emitting 14 W, 15 W, 5 W at the wavelengths of 1064 nm, 532 nm, and 355 nm, respectively. The backscattered light is collected by two telescopes, each having a diameter of 1.8 m. During nighttime the inelastic Raman scattered light at the wavelengths of 387 nm and 608 nm is recorded in addition to the light of the emitted wavelengths [11]. The wavelengths 387 nm and 608 nm were chosen as they are Raman scattered on Nitrogen only. We use the signal received at the emitted wavelengths and the Raman wavelengths to calculate backscatter ratios, as described in Langenbach et al. [15].

The backscatter ratio is the ratio of the detected signal originating from scattering processes on aerosol particles (Mie-scattering) and air molecules (Rayleigh-scattering) normalized by the contribution of molecular scattering only. Therefore, it contains information on the aerosol load in the scattering volume. For the discussion of the new retrieval approach, we have selected lidar measurements of March 2013, as these measurements are free of polar stratospheric clouds and free of enhanced aerosol due to volcanic eruptions or forest fires. Figure 1 shows the monthly mean

backscatter ratio profiles at 532 nm and 1064 nm for March 2013. This dataset is based on 55 h of lidar measurements during 7 days. The data was recorded with a temporal resolution of 30 s and a range resolution of 50 m. The lidar data was first processed with a time step of five minutes and a vertical resolution of 150 m to correct for instrumental effects (e.g., deadtime correction, noise removal). Backscatter ratios were then calculated with a time resolution of 1 h and a vertical resolution of 1 km. These data were then averaged for both systems and all data acquired in March 2013. About 30 h of observations were performed under daytime conditions where Raman signals are not available. To calculate backscatter ratios during these conditions, we use the nighttime Raman signals that were recorded in the same measurement run [15].

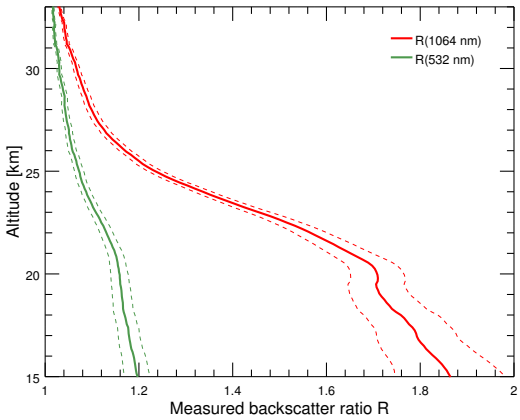

Figure 1. Monthly mean backscatter ratio profiles from lidar measurements during March 2013. Thick lines represent the mean values for the wavelengths 532 nm and 1064 nm. Dashed lines around the mean profiles indicate the error bands calculated as error of the mean.

3. Retrieval Approach

The main goal of this study is to describe an approach for the retrieval of vertical profiles of particle size and extinction of stratospheric sulfate aerosols from ground-based multi-color lidar observations. Because backscatter ratios at three wavelengths are available, a method for simultaneously inferring the log-normal distribution width and median radius from two color ratios was in earlier studies applied to lidar measurements of noctilucent clouds (e.g., [16,17]). This method is based on the exploitation of two color ratios determined from the lidar measurements at the three available wavelengths (355 nm, 532 nm, and 1064 nm). The method works well for the relatively small particles forming noctilucent clouds, with typical radii of several tens of nm, but it is not generally applicable to larger stratospheric aerosol particles. Instead, a simplified approach is used, which fixes one of the two parameters describing a monomodal log-normal particle size distribution (here, the distribution width) and retrieves the remaining one (the median radius) [18].

The retrieval—based on the assumptions described below—is performed in two steps. First, the aerosol median radius is determined by comparing the measured and modeled ratio of the backscatter ratio profiles at two different wavelengths. This can be done, because the color index for the wavelengths used depends on the median radius of the assumed log-normal size distribution. Second, the inferred particle median radius is employed in order to calculate aerosol extinction coefficient profiles from the measured backscatter ratio profiles. Finally, the aerosol particle number density can be determined.

3.1. Retrieval Assumptions

The aerosol is assumed to consist of 75% sulfuric acid (H_2SO_4) and 25% water, which defines its refractive index. For the assumed aerosol composition the real part of the refractive index is roughly $n_0^A(\lambda = 532) = 1.43$ at the wavelength of 532 nm and $n_0^A(\lambda = 1064) = 1.42$ at 1064 nm [19]. Note that the relative fractions of H_2SO_4 and H_2O of stratospheric sulfate aerosols are not constant, but will

vary depending on the ambient conditions. The fraction of sulfuric acid will be varied in Section 4 by 20% to examine its impact on the results and, therefore, quantify its contribution to the error budget. Such a variation should also represent the seasonal variability and a possible dependence on altitude. Aerosol absorption turned out to have only a minor influence on the retrieval, since the imaginary part of the refractive index is negligible and was, therefore, set to zero. Hence the scattering coefficients are identical to the extinction coefficients. Only the backscatter ratios at 1064 nm and 532 nm are used for the retrieval while the backscatter ratio at 355 nm is not used. At the wavelength of 355 nm the backscatter signals (in the altitude range of the stratospheric aerosol layer) are dominated by Rayleigh scattering and frequently used as a proxy for Rayleigh scattering [15].

The particle size distribution (PSD) is assumed to be monomodal log-normal:

$$\frac{dN_A(z,r,r_m(z),S)}{dr} = \frac{N_A(z)}{\sqrt{2\pi}\ln(S)r_m(z)} \cdot \exp\left(-\frac{(\ln(r)-\ln(r_m(z)))^2}{2\ln^2(S)}\right) \quad (1)$$

with r as the radius, $N_A(z)$ the number density of the aerosol particles, S the distribution width (geometric standard deviation) and $r_m(z)$ the median radius. (Note that the most important variables used are summarized in Table 1.) This assumption constitutes a clear simplification since multi-modal distributions seem to be common. Deshler [20], for example, directly measured a bi-modal aerosol distribution modelled by two log-normal modes. In particular, the second mode frequently seen in the in-situ OPC measurements by Deshler [20]—having a typical median radius of about 400 nm—has a significantly lower number density than the main mode with typical median radii of about 100 nm or less. For our work, a monomodal assumption is justified, even if further modes of very small particles are present because the measurement is dominated by the contribution of the main mode, as recently demonstrated by [14]. It also should be mentioned that, with every mode, additional parameters have to be taken into account. Since we have only one free parameter this approach would be not appropriate for our method.

Table 1. Symbols used throughout the article.

Symbol	Quantity	Unit
$R(z,r_m,\lambda)$	Backscatter ratio	dimensionless
$k^{sca}_{Mie}(z,r_m,\lambda)$	Mie scattering coefficient	km^{-1}
$k^{sca}_{Ray}(z,r_m,\lambda)$	Rayleigh scattering coefficient	km^{-1}
Θ	Scattering angle ($\Theta = 180°$ for lidar observations)	degrees
$P_{Mie}(\Theta,r_m,\lambda)$	Mie scattering phase function	sr^{-1}
$P_{Ray}(\Theta)$	Rayleigh scattering phase function	sr^{-1}
$\beta_{Mie}(z,r_m,\lambda)$	Mie volume scattering coefficient	$km^{-1} \cdot sr^{-1}$
$\beta_{Ray}(z,r_m,\lambda)$	Rayleigh volume scattering coefficient	$km^{-1} \cdot sr^{-1}$
$N_A(z)$	Aerosol particle number density	m^{-3}
$N(z)$	Air molecule number density	m^{-3}
$\sigma_{Mie}(r_m,\lambda)$	Mie scattering cross section	m^2
$\sigma_{Ray}(r_m,\lambda)$	Rayleigh scattering cross section	m^2
$r_m(z)$	Median aerosol radius	nm
λ	Wavelength	nm
z	Altitude	km
S	Particle size distribution width	dimensionless
$C(z,r_m,\lambda_1,\lambda_2)$	Color index from backscatter ratios	dimensionless

We assume that only the number density and median radius in Equation (1) are changing with altitude (z). Here, the assumption of the distribution width S becomes important. Because its value often covers a wide range between $S < 1.1$ up to $S \approx 1.7$, a value of $S = 1.5$ was chosen (e.g., [20,21]). We note that this value is somewhat arbitrary and has a direct impact on the values of the retrieved median radii. However, the impact on the inferred aerosol extinction coefficients is relatively weak (see

Section 4). Distribution widths other than 1.5 will only be used to determine the impact of a possible inaccurate assumption on the retrieval.

Given these assumptions, we can calculate, for example, a mean scattering cross section of the aerosol population as follows:

$$\langle \sigma_{Mie}(z,\lambda) \rangle = \int_0^\infty \frac{dN_A(z,r,r_m(z),S)}{dr} \cdot \sigma_{Mie}(r,\lambda,n_0^A(\lambda))\, dr. \tag{2}$$

To simplify the notation in the following, we define $\sigma_{Mie}(r_m,\lambda) := \langle \sigma_{Mie}(z,\lambda) \rangle$ and omit the dependence of $r_m(z)$ on altitude.

3.2. Retrieval of Aerosol Particle Size Information

In the first step particle size information is retrieved, which is a necessary requirement for further computations. The lidar backscatter ratio $R(z,r_m,\lambda)$ at altitude z and wavelength λ is given by

$$R(z,r_m,\lambda) = \frac{\beta_{Mie}(z,r_m,\lambda) + \beta_{Ray}(z,\lambda)}{\beta_{Ray}(z,\lambda)} \tag{3}$$

which can be simplified to

$$R(z,r_m,\lambda) = \frac{\beta_{Mie}(z,r_m,\lambda)}{\beta_{Ray}(z,\lambda)} + 1 \tag{4}$$

with the aerosol and Rayleigh volume backscatter coefficients $\beta_{Mie}(z,r_m,\lambda)$ and $\beta_{Ray}(z,\lambda)$ given by

$$\beta_{Mie}(z,r_m,\lambda) = k_{Mie}^{sca}(z,r_m,\lambda) \cdot P_{Mie}(\Theta,r_m,\lambda) \tag{5}$$

and

$$\beta_{Ray}(z,\lambda) = k_{Ray}^{sca}(z,\lambda) \cdot P_{Ray}(\Theta). \tag{6}$$

Here, k_{Mie}^{sca} and k_{Ray}^{sca} denote the Mie and Rayleigh scattering coefficients and P_{Mie} and P_{Ray} correspond to the phase functions for Mie and Rayleigh scattering. $\Theta = 180^\circ$ is the scattering angle. Equation (5) can be written as

$$\beta_{Mie}(z,r_m,\lambda) = N_A(z) \cdot \sigma_{Mie}(r_m,\lambda) \cdot P_{Mie}(\Theta,r_m,\lambda) \tag{7}$$

with $N_A(z)$ as the aerosol particle number density and $\sigma_{Mie}(r_m,\lambda)$ as the Mie scattering cross section [22]. Note that the scattering cross section depends implicitly on altitude through the altitude dependence of r_m. For Rayleigh scattering the analogous relationship is

$$\beta_{Ray}(z,\lambda) = N(z) \cdot \sigma_{Ray}(\lambda) \cdot P_{Ray}(\Theta) \tag{8}$$

with $N(z)$ as the air density and $\sigma_{Ray}(\lambda)$ as the Rayleigh scattering cross section [23]:

$$\sigma_{Ray}(\lambda) = \frac{24\pi^3}{\lambda^4 N_0^2} \frac{(n_0(\lambda)^2-1)^2}{(n_0(\lambda)^2+2)^2} \left(\frac{6+3\gamma(\lambda)}{6-7\gamma(\lambda)} \right). \tag{9}$$

Here, N_0 denotes the number density of air for standard conditions, $n_0(\lambda)$ is the refractive index of air for the given wavelength, also for standard conditions (with $n_0(532\,\text{nm}) = 1.0002782$ and $n_0(1064\,\text{nm}) = 1.0002739$), and $\gamma(\lambda)$ is the depolarisation factor of air.

Using lidar backscatter ratio measurements at two different wavelengths, a color index C can be formed:

$$C(z, r_m, \lambda_1, \lambda_2) = \frac{R(z, r_m, \lambda_1) - 1}{R(z, r_m, \lambda_2) - 1} = \frac{\beta_{Mie}(z, r_m, \lambda_1)}{\beta_{Mie}(z, r_m, \lambda_2)} \cdot \frac{\beta_{Ray}(z, \lambda_2)}{\beta_{Ray}(z, \lambda_1)} \quad (10)$$

with λ_1 = 1064 nm and λ_2 = 532 nm. Note that the color index C defined here should not be confused with the ratio of the Mie volume scattering coefficients at the two wavelengths, which is also often used and sometimes denoted by "color ratio" (e.g., [16]). It is worth pointing out that the color index $C(z, r_m, 1064\,\text{nm}, 532\,\text{nm})$ depends on altitude only through the altitude dependence of $r_m(z)$. The underlying reason is that the aerosol and air number densities in β_{Mie} and β_{Ray} cancel out when calculating the ratio. For β_{Ray}, also the phase function cancels out and the color index can be expressed as:

$$C\,(z, r_m, \lambda_1, \lambda_2) = \frac{\sigma_{Mie}(r_m, \lambda_1) P_{Mie}(\Theta, r_m, \lambda_1)}{\sigma_{Mie}(r_m, \lambda_2) P_{Mie}(\Theta, r_m, \lambda_2)} \cdot \frac{\sigma_{Ray}(\lambda_2)}{\sigma_{Ray}(\lambda_1)}. \quad (11)$$

It is worth keeping in mind that the color index implicitly depends on the assumptions about the aerosol refractive index and the particle size distribution introduced in Section 3.1. Figure 2 shows the altitude dependence of the color index determined from the monthly averaged backscatter ratio profiles of March 2013 (shown in Figure 1). The Mie-scattering cross sections $\sigma_{Mie}(r_m, \lambda)$ and Mie phase functions $P_{Mie}(\Theta, r_m, \lambda)$ used in the forward model (Equations (5) and (11)) are calculated using the `IDL` Mie scattering routines provided by the University of Oxford [24].

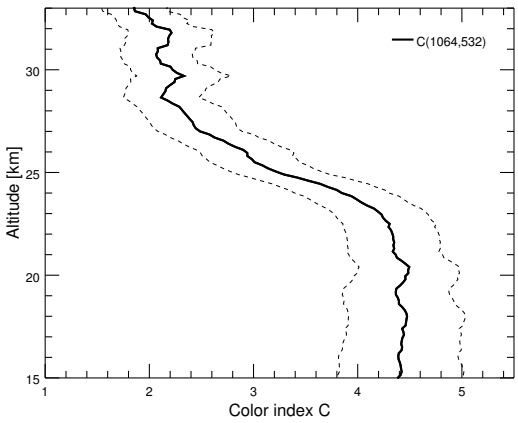

Figure 2. Color index profile calculated from monthly mean backscatter ratio profiles at the wavelengths of 1064 nm and 532 nm for March 2013 and using Equation (10). The thick line represents the mean value and the dashed lines indicate the error band calculated by Gaussian error propagation of the error of the mean backscatter ratio values.

Figure 3 shows the color index for different median radii r_m and for different widths (S) of the assumed monomodal log-normal PSD (Equation (1)). The color indices obtained from measurements in March 2013 are indicated by the red shaded area in Figure 3. The median radius r_m is then retrieved from the measured color index using linear interpolation to a precalculated lookup table of color indices as a function of r_m. This is done for every altitude allowing the determination of a vertical profile of the median radius.

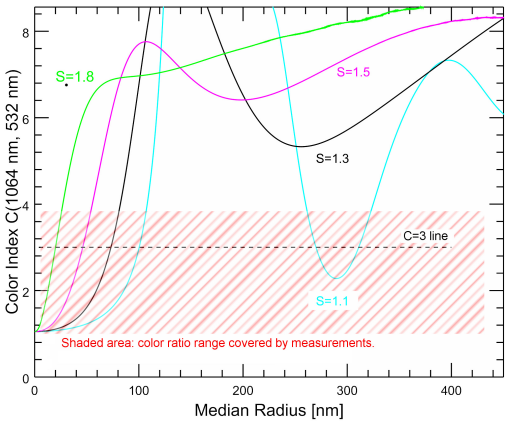

Figure 3. Radius dependence of the color index C for $\lambda_1 = 1064$ nm and $\lambda_2 = 532$ nm (see Equation (11)) calculated using a Mie scattering code for different distribution widths S (solid lines). The range of color ratios from monthly mean data of March 2013 is indicated by the shaded area. The horizontal black dashed line indicates a color index value of $C = 3$.

3.3. Radius Ambiguity

The radius assignment is not necessarily unique. Some of the measured color index values may be caused by multiple median radius values if the width (S) of the PSD is changing, as seen in Figure 3. For example, a color index value of $C = 3$ may be generated by PSDs with median radii of about $r_m = 75$ nm, $r_m = 45$ nm, and $r_m = 20$ nm for distribution widths of $S = 1.3$, $S = 1.5$, and $S = 1.8$. For distribution widths of less than about $S = 1.75$ the radius retrieval may be divided into different branches, i.e., radius ranges between neighboring local extrema of C. For $S = 1.5$ the first branch extends from $r_m = 0$ nm to about $r_m = 105$ nm, whereas branch 2 ranges from roughly $r_m = 105$ nm to $r_m = 200$ nm and branch 3 from $r_m = 200$ nm to roughly $r_m = 450$ nm. If the width of the PSD is (unrealistically) small ($S = 1.1$), a color index of $C = 3$ corresponds to radii of roughly $r_m = 100$ nm, $r_m = 270$ nm and $r_m = 310$ nm for the respective branches 1 to 3. Some branches are excluded from the retrieval based on the following considerations.

First, it should be noted that by increasing the assumed distribution width the computed color index curve changes its shape and some branches vanish. Above a distribution width of around $S = 1.75$, any ambiguity in the radius retrieval vanishes since the color index increases monotonic with r_m. In this context, it is worth pointing out that several studies report distribution widths well exceeding $S = 1.4$ [25–27].

Second, for the range of color index values measured by the lidar in March 2013, branches 2 and 3 are excluded for $S = 1.5$, as these branches do not produce the observed color index values. There are further contradictions when picking solutions from branches 2 and 3. These solutions would for example lead to very high minimal r_m values of several hundred nanometers without any transition to smaller values along the vertical profile. High color index values ($C \gg 4$) would be expected if particles grow or shrink from about 110 nm to 260 nm, and these high color index values are not observed. In Figure 4 we show the altitude dependence of the retrieved r_m for different S (and for branch 3 of $S = 1.1$) to illustrate this issue. We do not show results from branch 2 because the resulting median radii increase continuously with altitude, which seems to be physically implausible.

For the range of color index values observed by lidar, only the retrieval based on branch 1 gives plausible results for S larger than about 1.1. It is worth pointing out that color indices from branch 3 and $S = 1.1$ only agree to the measured color indices for altitudes below about 28 km. Above this altitude, the measured color indices are lower than the local minimum of C at about $r_m = 290$ nm (see Figure 3).

We see two reasons for excluding branch 3. First, very small distribution widths with $S \leq 1.1$ are not compatible with our data set, as we use monthly mean lidar data. Even for quiescent background conditions, the aerosol population can show a highly complex spatial structure with filaments and

a dynamic behavior on timescales of several hours [15]. Therefore, the assumption of an aerosol population with a very narrow distribution width during a relatively long period of one month is unrealistic. This argument is consistent with many in-situ and remote sensing studies [20,26–29]. Secondly, the absence of median radii below about 290 nm and a discrete jump of particle sizes around the altitude of 28 km from about 290 nm to about 100 nm does not characterize a physically plausible aerosol size profile.

It should be kept in mind that, for periods after large volcanic eruptions, larger particles are found in the aerosol layer [20]. In these cases, we would expect to see a variety of particle sizes at certain altitudes and hence a larger range of color index values than what we observed in March 2013. For a larger spread of color index values, the arguments for ruling out radius branches need to be revisited.

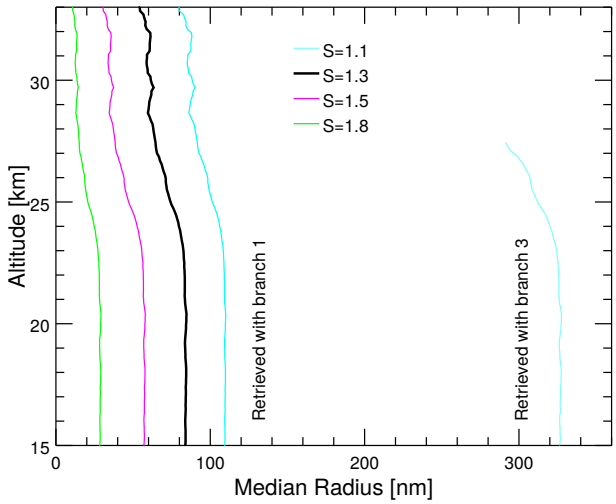

Figure 4. Retrieved median radius profiles based on branch 1 (curves on the left) and branch 3 (cyan curve on the right). The branch 1 retrievals are shown for different distribution widths S to illustrate its influence on the radius retrieval. For $S < 1.1$, a radius assignment using branch 3 exists for the altitude range up to about 28 km as shown in the rightmost profile. Shown are median radius profiles that are computed from monthly mean backscatter ratio profiles for March 2013.

3.4. Derivation of Extinction Profiles

Once the median radius is determined, the extinction profile is calculated by solving Equation (5) for k^{sca}_{Mie} and then substituting β_{Mie} from Equation (4) and making use of Equation (6):

$$k^{ext}_{Mie}(z, r_m, \lambda) = k^{sca}_{Mie}(z, r_m, \lambda) = \frac{k^{sca}_{Ray}(z, \lambda) \cdot P_{Ray}(\Theta)}{P_{Mie}(\Theta, r_m, \lambda)} \cdot (R(z, r_m, \lambda) - 1)\,. \tag{12}$$

The quantities on the right hand side of this equation are either measured (R) or known (P_{Ray}) or are calculated while using r_m (P_{Mie}). We calculate $k^{sca}_{Ray}(z, \lambda)$ by using air density from monthly means (of daily means) of temperature and pressure profiles taken from ERA-Interim reanalysis data provided by the European Centre for Medium-range Weather Forecast [30]. With those ingredients inserted into Equation (12), extinction profiles are computed for the two wavelengths studied here. Figure 5 shows the aerosol extinction profiles at 532 nm and 1064 nm based on monthly mean lidar measurements for March 2013. It is worth noting that Equation (12) can be rewritten as:

$$k^{sca}_{Mie}(z, r_m, \lambda) = \Lambda(r_m, \lambda) \cdot k^{sca}_{Ray}(z, \lambda) \cdot P_{Ray}(\Theta) \cdot (R(z, r_m, \lambda) - 1) \tag{13}$$

where Λ is the so-called lidar ratio:

$$\Lambda(r_m, \lambda) = \frac{k_{sca}(r_m, \lambda)}{\beta_{Mie}(\Theta, r_m, \lambda)} = \frac{1}{P_{Mie}(\Theta, r_m, \lambda)}. \tag{14}$$

The possibility to compute the lidar ratio from the retrieved median radius is an advantageous feature of the method applied here. In cases where Λ can not be inferred from the measurements (contrary to our approach), a constant lidar ratio with values around $\Lambda(\lambda = 532) \approx 50$ sr for 532 nm is often assumed (e.g., [31]). Based on Equation (14), the extinction profile is then calculated by:

$$k_{Mie}^{sca}(z, \lambda) = \Lambda(\lambda) \cdot \beta_{Mie}(\Theta, z, \lambda). \tag{15}$$

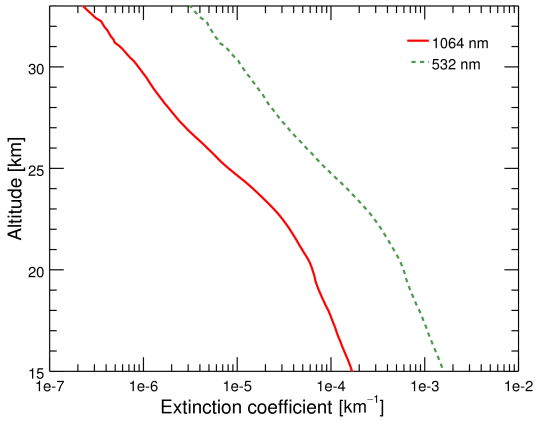

Figure 5. Extinction coefficient profiles derived from the monthly mean backscatter ratio profiles for March 2013 with an assumed distribution width of S = 1.5.

This approach—based on an assumed lidar ratio—constitutes the only way to estimate aerosol extinction coefficients if aerosol backscatter coefficients are available only at a single wavelength. However, assuming a constant lidar ratio $\Lambda(\lambda)$ does not account for its dependence on the radius, and therefore on its implicit dependence on altitude. The lidar ratio profile in Figure 6 shows that the assumption of a constant lidar ratio can be a good approximation for 1064 nm over the whole altitude range and for 532 nm for an altitude range between 15 and 23 km for the latitude and month studied here. The different behaviour for the two wavelengths is due to the weaker dependence of the phase function on radius for backscattering of the longer wavelength. For altitudes that are above 23 km the lidar ratio for 532 nm changes significantly, therefore leading to inevitable errors if its value is assumed to be constant.

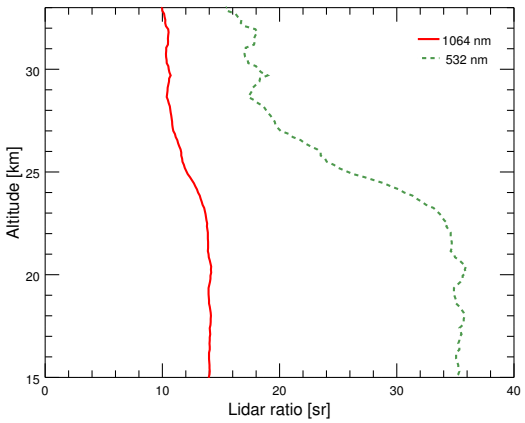

Figure 6. Stratospheric aerosol lidar ratio profile derived from measurements during March 2013 with an assumed distribution width of S = 1.5.

We note that in most studies on lidar measurements of stratospheric aerosols a constant lidar ratio is employed. Trickl et al. [32], e.g., assume a value of 50 sr, which was based on EARLINET results ([33]). However, Mattis et al. [33] only deal with tropospheric aerosols and it is not clear why the same lidar ratio should also be applicable to stratospheric aerosols. Khaykin et al. [31] also assume a lidar ratio of 50 sr (at 532 nm) for the volcanically quiescent period after 1997, following Trickl et al. [32]. Sakai et al. [34] employ lidar ratios between 35 and 50 sr, based on in-situ measurements of stratospheric aerosol particle size distributions at midlatitudes in both hemispheres. Stratospheric aerosol particle size parameters—and hence the lidar ratio—will certainly depend on latitude to a certain extent, implying that the lidar ratios reported in this study may not be directly applicable to the geolocations of other lidar stations. However, the value of the lidar ratio of stratospheric sulfate aerosols—as well as its variability with location, time, and particularly altitude—should be critically investigated, particularly because it directly affects the derived aerosol extinction coefficients and optical depth, the latter of which is often used to quantify radiative forcing.

3.5. Particle Number Density Estimation

Together with the extinction profiles retrieved in the previous section, all information is available to estimate the aerosol number density N_A utilising the relationship between extinction coefficient, scattering cross section, and particle number density. Following Equations (7) and (14), the particle number density is calculated as:

$$N_A(z) = \frac{k^{sca}_{Mie}(z,\lambda)}{\sigma_{Mie}(r_m,\lambda)}. \tag{16}$$

The aerosol number density profiles can now be computed from extinction coefficient profiles at both wavelengths. As can be seen in Figure 7, these two number density profiles are identical, as expected.

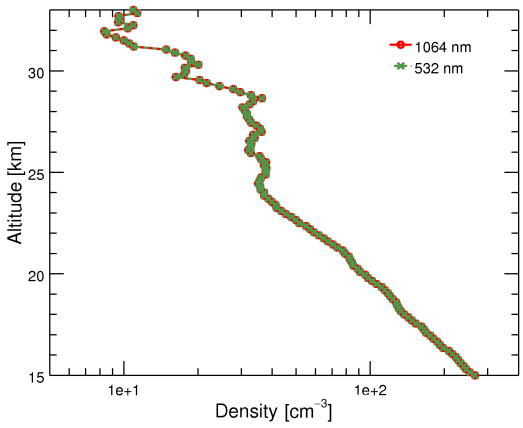

Figure 7. Stratospheric aerosol particle number density profiles for March 2013 with an assumed distribution width of S = 1.5 obtained from the extinction coefficient profiles at 532 nm and 1064 nm shown in Figure 5.

4. Error Estimation

A key point of the retrieval approach employed here is a correct determination of the median radius, since all inferred quantities depend on it. Therefore, we first investigate the impact of the assumptions and the measurement errors on r_m. The aerosol extinction and the particle number density also depend on atmospheric temperature and pressure through k^{sca}_{Ray}.

The retrieval was performed with perturbed parameter values used in the forward model in order to determine the impact of the distribution width (S) and the refractive index ($n^A_0(\lambda)$) on the median radius. The distribution width was varied by $\Delta S = \pm 0.1$ and $\Delta S = \pm 0.2$ and the refractive index was

varied by $\Delta n_0^A = \pm 0.04$. This value for the refractive index perturbation roughly corresponds to a 20% change of the H_2SO_4 concentration.

Figure 8 shows the contribution of each parameter to the error in r_m. The most significant impact on the radius determination comes from an incorrect assumption on the distribution width. A difference of $\Delta S = \pm 0.2$ leads to relative errors between roughly $\Delta r_m / r_m = \mp 40\%$ and ∓ 70, depending on altitude. If the assumed distribution width is increased, then the retrieved median radius decreases and vice versa. In Figure 9, we show the retrieved radius r_m and the combined error bands when adding the different errors, but separated for the two different assumptions of ΔS.

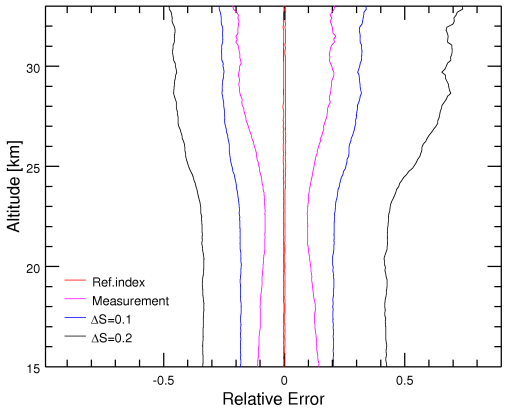

Figure 8. Relative error of the median radius $\Delta r_m / r_m$ due to measurement errors, uncertainties in the distribution width (ΔS), and the aerosol refractive index ($\Delta n_0^A = \pm 0.04$) for measurements of March 2013.

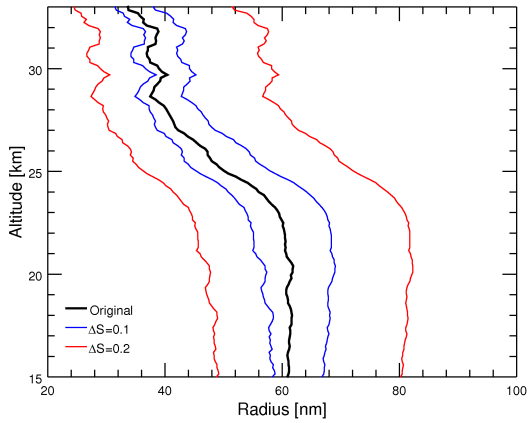

Figure 9. Median radius (r_m) profile for March 2013 inferred with an assumed distribution width of $S = 1.5$ (black curve). The error ranges are obtained by adding the error contributions of measurement uncertainty, refractive index variation, and uncertainties in the distribution widths (red and blue lines).

For the error estimation of the extinction coefficients, we also allow for uncertainties of temperature ($\Delta T \pm 1$ K) and pressure ($\Delta p / p = \pm 1\%$), since they are implicitly included in k_{Ray}^{sca}. The contributions of the different error sources to the relative error of the aerosol extinction coefficients ($\Delta k_{Mie}^{sca} / k_{Mie}^{sca}$) are shown in Figure 10. Again, the dominant contribution comes from an erroneous assumption of the distribution width. However, the relative error is not as big as in the case of the radius retrieval (Figure 8) and the inferred extinction coefficients seem to be rather robust against variations of the distribution width. This is also illustrated in Figure 11, which shows the extinction coefficient profiles together with the total error. Like in Figure 9 two error ranges are given for the two assumed errors of the distribution width of $\Delta S = \pm 0.1$ and $\Delta S = \pm 0.2$. The same procedure allows for an analogous calculation of the error bands for the lidar ratio profiles (Figure 6) displayed in Figure 12.

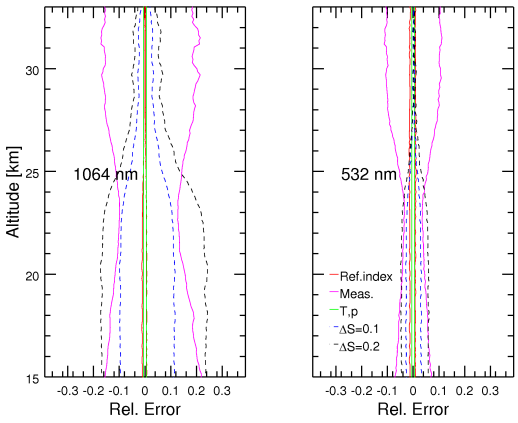

Figure 10. Relative error of the extinction coefficients ($\Delta k^{sca}_{Mie}/k^{sca}_{Mie}$) at the two wavelengths 1064 nm and 532 nm. The impact of uncertainties in refractive index, temperature, pressure, distribution width (ΔS) and measurement errors are shown for monthly mean measurements of March 2013.

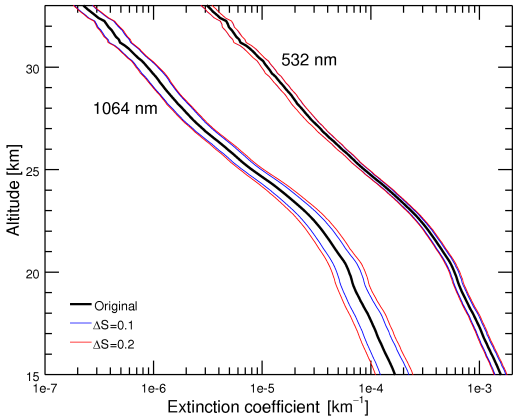

Figure 11. Extinction coefficient profiles (k^{sca}_{Mie}) for March 2013 inferred with an assumed distribution width of S = 1.5 (Original) with total error ranges of the two assumed deviations (ΔS) of the distribution width.

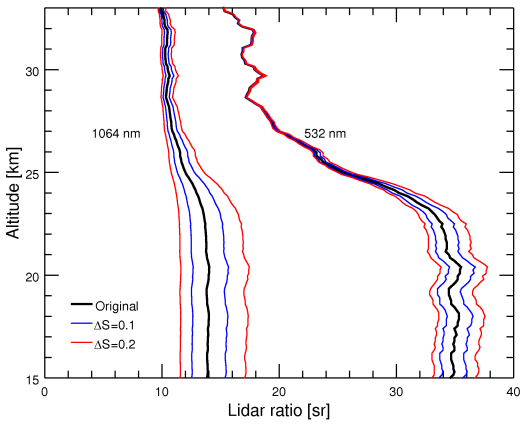

Figure 12. Lidar ratio profiles for March 2013 for an assumed distribution width of S = 1.5 (Original) with total error ranges of the two assumed deviations ΔS of the distribution width.

Finally, we show the error of the aerosol number density (N_A) in Figure 13. The number density is very sensitive to uncertainties of r_m as $\sigma_{Mie}(r_m, \lambda)$ in Equation (16) depends exponentially on r_m with about $\sigma_{Mie}(r_m, \lambda) \propto r_m^{\kappa}$ with κ of 4 to 5 (e.g., [14]).

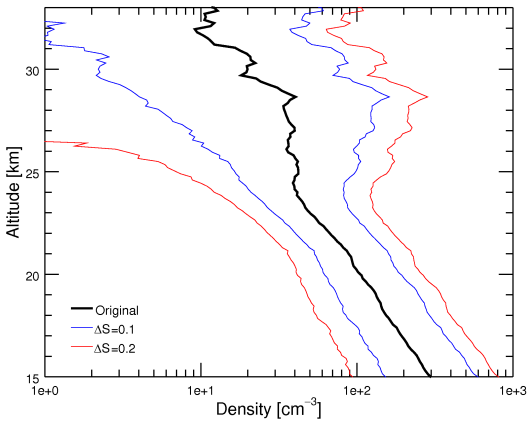

Figure 13. Aerosol number density profile (N_A) for March 2013 inferred with an assumed distribution width of S = 1.5 (Original). Blue and red lines indicate the total error ranges of the two assumed deviations (ΔS) of the distribution width.

5. Comparison with Independent Observations

This section deals with two different aspects. In Section 5.1, the retrieved median radii of stratospheric sulfate aerosol particles are compared to (not collocated) results from the literature. Section 5.2 presents comparisons of the retrieved aerosol extinction profiles with available satellite data sets.

5.1. Comparison of Particle Size Retrievals

The number of available studies on the size of stratospheric sulfate particles at high latitudes is rather small. Here, we limit the considerations to comparisons with non-collocated observations described in the literature.

McLinden et al. [26] employed polarized limb-radiance measurements with the CPFM (Composition and Photodissociative Flux Measurement) spectroradiometer operated on NASA's ER-2 high altitude aircraft during two field campaigns in April and May 1997. Both flights started in Fairbanks, Alaska (65° N, 148° W), and covered the high latitude American sector. For the retrieval of aerosol particle size information CPFM limb scans at latitudes of 83° N and 75° N were used. For their aerosol retrieval, an altitude independent monomodal log-normal PSD was assumed, which the authors claimed to be representative of the aerosol at all heights in the lower stratosphere covered by the measurements. Median radii of $r_m = 120 \pm 20$ nm and 100 ± 20 nm were retrieved at the two latitudes. The distribution width was given as logarithmic standard deviation (with values of 0.44 ± 0.04 and 0.46 ± 0.04) corresponding to distribution widths (geometric standard deviations) of $S = 1.55 \pm 0.06$ at 83° N and $S = 1.58 \pm 0.06$ at 75° N.

Bourassa et al. [25] retrieved stratospheric aerosol particle size information from OSIRIS limb-scatter measurements at 750 nm and 1530 nm, also assuming a monomodal log-normal PSD. From a single limb-scan (assuming $S = 1.6$) the authors retrieved a median radius (the article incorrectly states *mode* radius), decreasing from about 100 nm at 21 km to about 30 nm at 30 km altitude. The measurement was performed on 5 January 2004 at 35.6° S latitude and 112.6° longitude.

Ugolnikov et al. [27] presented stratospheric aerosol particle size retrievals from ground-based multi-spectral twilight measurements carried out with an all-sky camera in central Russia (55.2° N, 37.5° E) in spring and summer 2016, i.e., for volcanically relatively quiescent conditions. The authors assumed a monomodal log-normal PSD and retrieved an aerosol radius of about $r_m = 80$ nm and a width of $S = 1.5$–1.6.

Bingen et al. [21] and Bingen at al. [35] retrieved stratospheric aerosol particle size information from SAGE II solar occultation measurements for the period from 1985 to 2000. The retrieved aerosol radii are on the order of 200–350 nm at an altitude of 22.5 km in 1999, i.e., eight years after the eruption

of Mt. Pinatubo, when the stratospheric aerosol load was again close to background conditions. However it is important to mention that the PSDs are rather narrow, with retrieved $S \leq 1.1$.

Deshler [20] retrieved stratospheric aerosol particle size from balloon-borne measurements above Laramie (Wyoming, USA, 41° N, 105° W). This analysis considered a bimodal size distribution which may be present, even at background aerosol conditions. Averaged profiles obtained between 1995 and 2003 with reduced or without volcanic aerosol load from Pinatubo show an increase of the median radius of the main mode from roughly 45 nm at 16 km up to a maximum of 80 nm at 21 km with a distribution width of $S = 1.37$. For the time period with volcanic aerosols a maximal median radius of the main mode is found to be around 180 nm with $S = 1.41$.

In summary, a majority of the studies on the size of stratospheric sulfate aerosols yields—under volcanically quiescent conditions—median radii on the order of about 100 nm, in good overall agreement with the retrievals that are presented here. The exception are size retrievals based on multi-spectral solar occultation measurements with SAGE II [21,35,36] yielding mode (or median radii) of several hundred nm, even in the late 1990s, when the Pinatubo aerosol has already almost entirely disappeared. The discrepancies between the aerosol size parameters retrieved from SAGE II solar occultation measurements to the other techniques may in part be a consequence of different sensitivities of these measurement techniques to the aerosol particle population in combination with errors in the assumed PSD. von Savigny and Hoffmann [14] recently investigated this aspect. They simulated color index measurements for lidar backscatter and solar occultation measurement geometries assuming a bi-modal log-normal aerosol PSD (following the results by Desher et al. [28] and Deshler [20]) and retrieved the median radius of an assumed monomodal log-normal PSD with fixed width parameter. The median radii retrieved from the simulated solar occultation measurements are up to a factor of 3 larger than the radii retrieved for the lidar geometry—the main reason being that solar occultation measurements have a higher intrinsic sensitivity to the larger particles of the particle population.

The study also showed that the aerosol number density retrieved from the lidar measurements will be systematically larger than the one retrieved from solar occultation measurements—by up to factor of 50 for the assumptions made in [14]. This is also consistent with the aerosol number densities retrieved in the current study (see Figure 7) being systematically larger (by 1–2 orders of magnitude) than the aerosol number densities that are typically retrieved from solar occultation measurements, which are typically on the order of a few particles cm^{-3}.

5.2. Comparison of Extinction Profiles

In this section, the extinction coefficient profiles retrieved from the measurements with the ALOMAR lidar are compared to aerosol extinction profiles retrieved from measurements with different satellite instruments. Because the main focus of this study is on the retrieval methodology, we limit the comparison to observations from two different satellite instruments, namely OSIRIS and OMPS.

The OSIRIS (Optical Spectrograph and InfraRed Imager System) was launched in 2001 on-board the Swedish/Canadian/Finish/French Odin satellite [37,38]. OSIRIS performs limb-scatter observations in the 280–800 nm spectral range, allowing to retrieve stratospheric aerosol extinction profiles [39]. Aerosol extinction is provided at a wavelength of 750 nm and data version 5.07 is used here. OMPS (Ozone Mapping Profiling Suite) was launched in 2012 on-board the Suomi-NPP (Suomi National Polar-orbiting Partnership) satellite and performs nadir and limb-scatter measurements (e.g., [40]). Stratospheric aerosol extinction profiles are retrieved from limb-scatter measurements and tbey are provided at a wavelength of 675 nm (data version 1) [41].

For comparison, monthly mean and zonally averaged data for March 2013 in the latitude range 60° N–80° N were used. Measurements performed in March should not be influenced by polar stratospheric clouds which frequently appear during winter months. Prior to the comparison the extinction profiles measured at the two wavelengths 1064 nm and 532 nm have to be converted to the wavelengths for which the satellite data are provided. This conversion is done using the Ångström approach [42].

$$k_{Mie}^{ext}(z, r_m, \lambda) = c(z) \cdot \lambda^{-\alpha(r_m)} \tag{17}$$

with the Ångström exponent $\alpha(r_m)$, a proportionality factor $c(z)$ (depending on the aerosol number density) and λ denoting the wavelength. Because our retrieval provides extinction coefficient profiles at two wavelengths ($\lambda_1 = 532\,\text{nm}$ and $\lambda_2 = 1064\,\text{nm}$) the Ångström exponent is obtained by:

$$\alpha(r_m) = \frac{\ln(k_{Mie}^{ext}(z, r_m, \lambda_2)) - \ln(k_{Mie}^{ext}(z, r_m, \lambda_1))}{\ln(\lambda_1) - \ln(\lambda_2)}. \tag{18}$$

It is worth pointing out that $\alpha(r_m)$ depends on altitude through r_m. As discussed earlier, the altitude dependence of $r_m = r_m(z)$ is omitted to simplify the notation.

Figure 14 shows a comparison between the satellite observations and the lidar extinction profiles converted from the 532 nm profile to the corresponding satellite wavelength. The shapes and values of both profiles look very similar for altitudes below roughly 25 km. However, above this altitude, the OSIRIS profile shows a pronounced dip-like structure. This behaviour is probably caused by a low bias in the OSIRIS aerosol extinction retrievals at high latitudes and altitudes. This bias appears from time to time and is a known issue [43]. Although the comparison looks quite good, it is worth pointing out that the measurements are not performed at exactly the same time and location.

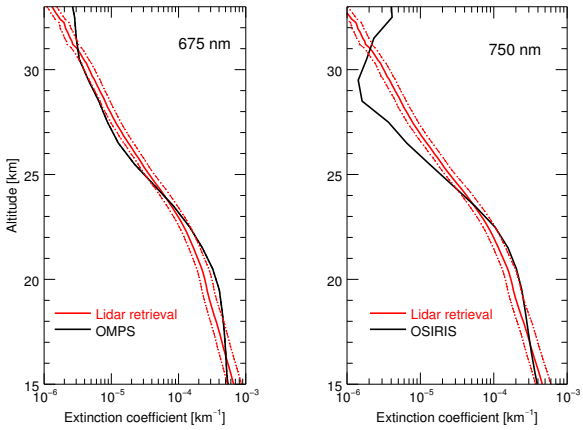

Figure 14. Extinction profiles obtained from the OMPS (**left**) and OSIRIS (**right**) instruments for March 2013. The red solid lines show the lidar extinction profile for March 2013 retrieved with S = 1.5 and converted to the wavelengths of OMPS and OSIRIS using Equation (17). The red dotted lines indicate the error ranges (similar to Figure 11).

6. Conclusions

In this work, we presented an approach for retrieving particle size and extinction coefficient profiles of stratospheric aerosols from multi-color measurements with the ALOMAR-RMR lidar in northern Norway. The retrieval approach is based on comparing the measured and modeled color indices for the wavelengths 1064 nm and 532 nm. In a first retrieval step profiles of the aerosol median radius of a monomodal log-normal particle size distribution with fixed width are obtained. These are used in a second step, together with temperature and air density profiles from ERA-Interim, to calculate the desired aerosol extinction profiles. Although assumptions on the aerosol properties have to be made, the inferred extinction coefficients are relatively robust against variations of the assumed distribution width. The direct comparison with extinction coefficient profiles obtained by satellite-borne measurements show a significant relative difference of roughly 40% at altitudes around 20 km, which in the case of OSIRIS can reach over 100% at higher altitudes. As pointed out, this high deviation is probably caused by a known low bias of the aerosol extinction retrieved from OSIRIS measurements at high northern latitudes and the respective altitudes.

To our best knowledge this study describes a novel approach and presents the first combined retrieval of median radius $r_m(z)$, number density $N_A(z)$, and extinction $k_{Mie}^{sca}(z)$ of stratospheric aerosols based on ground-based lidar measurements. A detailed investigation of error sources shows that the distribution width constitutes the dominant error source for the retrieval. The median radii of the aerosol size distribution obtained with this approach are in good overall agreement with other independent particle size observations (except those by SAGE II) which confirms that our assumptions are valid.

Author Contributions: C.v.S. and J.Z. developed and implemented the described method with the help of G.B. A.L., G.B. and F.-J.L. provided the lidar measurement data, A.B. provided the OSIRIS satellite data. All authors discussed the content of the paper, edited and proofread it. All authors have read and agreed to the published version of the manuscript.

Funding: This work was funded by the Deutsche Forschungsgemeinschaft (DFG, grant number 312991878).

Acknowledgments: We are thankful for valuable input from Michael Gerding and Jens Fiedler. We also thank the OMPS-LP team for providing the stratospheric aerosol extinction profiles used in this study.

Conflicts of Interest: The authors declare that they have no conflict of interest.

References

1. Kremser, S.; Thomason, L.W.; von Hobe, M.; Hermann, M.; Deshler, T.; Timmreck, C.; Toohey, M.; Stenke, A.; Schwarz, J.P.; Weigel, R.; et al. Stratospheric aerosol—Observations, processes and impact on climate. *Rev. Geophys.* **2016**, *54*, 278–335. [CrossRef]
2. von Savigny, C.; Timmreck, C.; Buehler, S.A.; Burrows, J.P.; Giorgetta, M.A.; Hegerl, G.; Hoose, C.; Quaas, J.; Malinina, E.; Rozanov, A.; et al. The Research Unit VolImpact: Revisiting the volcanic impact on atmosphere and climate—Preparations for the next big volcanic eruption. *Met. Z.* **2020**, *29*, 3–18. [CrossRef]
3. Crutzen, P.J. The possible importance of CSO for the sulfate layer of the stratosphere. *Geophys. Res. Lett.* **1976**, *3*, 73–76. [CrossRef]
4. Timmreck, C. Modeling the climatic effects of large volcanic eruptions. *WIREs Clim. Chang.* **2012**, *3*, 545–564. [CrossRef]
5. Curtius, J.; Weigel, R.; Vössing, H.-J.; Wernli, H.; Werner, A.; Volk, C.-M.; Konopka, P.; Krebsbach, M.; Schiller, C.; Roiger, A.; et al. Observations of meteoric material and implications for aerosol nucleation in the winter Arctic lower stratosphere derived from in situ particle measurements. *Atmos. Chem. Phys.* **2005**, *5*, 3053–3069. [CrossRef]
6. Robock, A. Volcanic Eruptions and Climate. *Rev. Geophys.* **2000**, *38*, 191–219. [CrossRef]
7. Dutton, E.G.; Christy, J.R. Solar radiative forcing at selected locations and evidence for global lower tropospheric cooling following the eruptions of El Chichon and Pinatubo. *Geophys. Res. Lett.* **1992**, *19*, 2313–2316. [CrossRef]
8. Brasseur, G.; Granier, C. Mount Pinatubo aerosols, chlorofluorocarbons, and ozone depletion. *Science* **1992**, *25*, 1239–1242. [CrossRef]
9. Tie, X.; Brasseur, G. The response of stratospheric ozone to volcanic eruptions: Sensitivity to atmospheric chlorine loading. *Geophys. Res. Lett.* **1995**, *22*, 3035–3038. [CrossRef]
10. Langematz, U.; Tully, M.; Calvo, N.; Dameris, M.; de Laat, A.T.J.; Klekociuk, A.; Müller, R.; Young, P. *Polar Stratospheric Ozone: Past, Present, and Future, Chapter 4 in Scientific Assessment of Ozone Depletion: 2018, Global Ozone Research and Monitoring Project—Report No. 58*; World Meteorological Organization: Geneva, Switzerland, 2018.
11. von Zahn, U.; von Cossart, G.; Fiedler, J.; Fricke, K.H.; Nelke, G.; Baumgarten, G.; Rees, D.; Hauchecorne, A.; Adolfsen, K. The ALOMAR Rayleigh/Mie/Raman lidar: Objectives, configuration and performance. *Ann. Geophys.* **2000**, *18*, 815–833. [CrossRef]
12. Blum, U.; Khosrawi, F.; Baumgarten, G.; Stebel, K.; Müller, R.; Fricke, K.H. Simultaneous lidar observations of a polar stratospheric cloud on the east and west sides of the scandinavian mountains and microphysical box model calculations. *Ann. Geophys.* **2006**, *24*, 3267–3277. [CrossRef]
13. Jumelet, J.; Bekki, S.; David, C.; Keckhut, P. Statistical estimation of stratospheric particle size distribution by combining optical modelling and lidar scattering measurements. *Atmos. Chem. Phys.* **2008**, *8*, 5435–5448. [CrossRef]

14. von Savigny, C.; Hoffmann, C. Issues related to the retrieval of stratospheric-aerosol particle size information based on optical measurements. *Atmos. Meas. Tech.* **2020**, *13*, 1909–1920. [CrossRef]
15. Langenbach, A.; Baumgarten, G.; Fiedler, J.; Lübken, F.-J.; von Savigny, C.; Zalach, J. Year-round stratospheric aerosol backscatter ratios calculated from lidar measurements above Northern Norway. *Atmos. Meas. Tech.* **2019**, *12*, 4065–4076. [CrossRef]
16. von Cossart, G.; Fiedler, J.; von Zahn, U. Size distributions of NLC particles as determined from 3-color observations of NLC by ground-based lidar. *Geophys. Res. Lett.* **1999**, *26*, 1513–1516. [CrossRef]
17. Baumgarten, G.; Fiedler, J.; von Cossart, G. The size of noctilucent cloud particles above ALOMAR (69N,16E): Optical modeling and method description. *Adv. Space Res.* **2007**, *40*, 772–784. [CrossRef]
18. Yue, G.K.; Deepak, A. Retrieval of stratospheric aerosol size distribution from atmospheric extinction of solar radiation at two wavelengths. *Appl. Opt.* **1983**, *22*, 1639–1645. [CrossRef]
19. Palmer, K.F.; Williams, D. Optical Constants of Sulfuric Acid; Application to the Clouds of Venus. *Appl. Opt.* **1975**, *14*, 208–219. [CrossRef]
20. Deshler, T. A review of global stratospheric aerosol: Measurement, importance, life cycle, and local stratospheric aerosol. *Atmos. Res.* **2008**, *90*, 223–232. [CrossRef]
21. Bingen, C.; Fussen, D.; Vanhellemont, F. A global climatology of stratospheric aerosol size distribution parameters derived from SAGE II data over the period 1984–2000: 1. Methodology and climatological observations. *J. Geophys. Res.* **2004**, *109*, D06201. [CrossRef]
22. Bohren, C.F.; Huffman, D.R. *Absorption and Scattering of Light by Small Particles*; Wiley Science Paperback Series; Wiley Professional Paperback Edition: Hoboken, NJ, USA, 1998.
23. Bucholtz, A. Rayleigh-scattering calculations for the terrestial atmosphere. *Appl. Opt.* **1995**, *34*, 2765–2773. [CrossRef] [PubMed]
24. Mie Scattering Routines, University of Oxford, Departement of Physics. Available online: http://eodg.atm.ox.ac.uk/MIE/index.html (accessed on 31 December 2018).
25. Bourassa, A.E.; Degenstein, D.A.; Llewellyn, E.J. Retrieval of stratospheric aerosol size information from OSIRIS limb scattered sunlight spectra. *Atmos. Chem. Phys.* **2008**, *8*, 6375–6380. [CrossRef]
26. McLinden, C.A.; McConnell, J.C.; McElroy, C.T.; Griffioen, E. Observations of stratospheric aerosol using CPFM polarized limb radiances. *J. Atmos. Sci.* **1999**, *56*, 233–240. [CrossRef]
27. Ugolnikov, O.S.; Maslov, I.A. Investigations of the Background Stratospheric Aerosol Using Multicolor Wide-Angle Measurements of the Twilight Glow Background. *Cosm. Res.* **2018**, *56*, 85–93. [CrossRef]
28. Deshler, T.; Hervig, M.E.; Hofmann, D.J.; Rosen, J.M.; Liley, J.B. Thirty years of in situ stratospheric aerosol size distribution measurements from Laramie, Wyoming (41° N), using balloon-borne instruments. *J. Geophys. Res.* **2003**, *108*, 4167. [CrossRef]
29. Wrana, F. Charakterisierung der Größenverteilung Stratosphärischer Aerosole Mittels Multispektraler Satellitengestützter Extinktionsmessungen. Master's Thesis, Institute of Physics, University of Greifswald, Greifswald, Germany, 2019.
30. European Centre for Medium-Range Weather Forecasts (ECMWF). The ERA-Interim Reanalysis Dataset, Copernicus Climate Change Service (C3S). Available online: https://apps.ecmwf.int/datasets/data/interim-full-moda/levtype=pl/ (accessed on 15 January 2019).
31. Khaykin, S.M.; Godin-Beekmann, S.; Keckhut, P.; Hauchecorne, A.; Jumelet, J.; Vernier, J.P.; Bourassa, A.; Degenstein, D.A.; Rieger, L.A.; Bingen, C.; et al. Variability and evolution of the midlatitude stratospheric aerosol budget from 22 years of ground-based lidar and satellite observations. *Atmos. Chem. Phys.* **2017**, *17*, 1829–1845. [CrossRef]
32. Trickl, T.; Giehl, H.; Jäger, H.; Vogelmann, H. 35 yr of stratospheric aerosol measurements at Garmisch-Partenkirchen: From Fuego to Eyjafjallajökull. *Atmos. Chem. Phys.* **2013**, *13*, 5205–5225. [CrossRef]
33. Mattis, I.; Ansmann, A.; Müller, D.; Wandinger, U.; Althausen, D. Multiyear aerosol observations with dualwavelength Raman lidar in the framework of EARLINET. *J. Geophys. Res.* **2004**, *109*, D132035. [CrossRef]
34. Sakai, T.; Uchino, O.; Nagai, T.; Liley, B.; Morino, I.; Fujimoto, T. Longterm variation of stratospheric aerosols observed with lidars over Tsukuba, Japan, from 1982 and Lauder, New Zealand, from 1992 to 2015. *J. Geophys. Res. Atmos.* **2016**, *121*, 283–293. [CrossRef]
35. Bingen, C.; Fussen, D.; Vanhellemont, F. A global climatology of stratospheric aerosol size distribution parameters derived from SAGE II data over the period 1984–2000: 2. Reference data. *J. Geophys. Res.* **2004**, *109*, D06202. [CrossRef]

36. Bingen, C.; Vanhellemont, F.; Fussen, D. A new regularized inversion method for the retrieval of stratospheric aerosol size distributions applied to 16 years of SAGE II data (1984–2000): Method, results and validation. *Ann. Geophys.* **2003**, *21*, 797–804. [CrossRef]
37. Llewellyn, E.J.; Lloyd, N.D.; Degenstein, D A.; Gattinger, R.L.; Petelina, S.V.; Bourassa, A.E.; Wiensz, J.T.; Ivanov, E.V.; McDade, I.C.; Solheim, B.H.; et al. The OSIRIS instrument on the Odin satellite. *Can. J. Phys.* **2004**, *82*, 411–422. [CrossRef]
38. Murtagh, D.; Frisk, U.; Merino, F.; Ridal, M.; Jonsson, A.; Stegman, J.; Witt, G.; Eriksson, P.; Jiménez, C.; Megie, G.; et al. An overview of the Odin Atmospheric Mission. *Can. J. Phys.* **2002**, *80*, 309–319. [CrossRef]
39. Bourassa, A.E.; Rieger, L.A.; Lloyd, N.D.; Degenstein, D.A. Odin-OSIRIS stratospheric aerosol data product and SAGE III intercomparison. *Atmos. Chem. Phys.* **2012**, *12*, 605–614. [CrossRef]
40. Jaross, G.; Bhartia, P.K.; Chen, G.; Kowitt, M.; Haken, M.; Chen, Z.; Xu, P.; Warner, J.; Kelly, T.; OMPS Limb Profiler instrument performance assessment. *J. Geophys. Res. Atmos.* **2014**, *119*, 4399–4412. [CrossRef]
41. DeLand, M.; Bhartia, P.; Xu, P.; Zhu, T. OMPS Limb Profiler Aerosol Extinction Product AER675: Version 0.5 Product Description. Available online: https://ozoneaq.gsfc.nasa.gov/media/docs/OMPS_LP_AER675_V0.5_Product_Description.pdf (accessed on 15 January 2019).
42. Angström, A. On the atmospheric transmission of Sun radiation and on dust in the air. *Geogr. Ann.* **1929**, *11*, 156–166.
43. Rieger, L.; Bourassa, A.; Degenstein, D. Merging the OSIRIS and SAGE II stratospheric aerosol records. *J. Geophys. Res. Atmos.* **2015**, *120*. [CrossRef]